



Effect of artificial aggregate shapes on the porosity, tortuosity and permeability of their packings

N.A. Conzelmann^{a,b}, M.N. Partl^b, F.J. Clemens^b, C.R. Müller^{a,*}, L.D. Poulikakos^b

^a ETH Zürich, Laboratory of Energy Science and Engineering, Department of Mechanical and Process Engineering, Institute of Energy and Process Engineering, Leonhardstrasse 21, 8092 Zürich, Switzerland

^b Empa – Swiss Federal Laboratories for Materials Science and Technology, Überlandstrasse 129, 8600 Dübendorf, Switzerland

ARTICLE INFO

Article history:

Received 13 July 2021

Received in revised form 3 November 2021

Accepted 23 November 2021

Available online 29 November 2021

Keywords:

Artificial aggregates

Aggregate shape

Non-convex shapes

Porosity

Permeability

Construction materials

ABSTRACT

Natural aggregates such as gravel are used in many construction applications for which porous structures are needed, for example to allow water drainage. However, the range of attainable porosities is limited due to the irregular shapes of natural aggregates. Here we investigate artificial aggregates of engineered shapes, which allow structures with porosities exceeding 0.7. In this study packings of a variety of artificial aggregate shapes are examined by both numerical and experimental techniques. We can establish a correlation between the porosity of a packing and the sphericity of the aggregates. Furthermore, we confirm that the Carman-Kozeny correlation can be used to predict accurately the permeability of a packing for a wide range of porosities (0.33–0.78). Establishment of this basic relationship between the porosity and permeability of a packing is critical for the design of artificial aggregates for novel applications such as energy harvesting from pavements.

© 2021 The Authors. Published by Elsevier B.V. This is an open access article under the CC BY-NC-ND license (<http://creativecommons.org/licenses/by-nc-nd/4.0/>).

1. Introduction

Aggregates in the form of sand, gravel or crushed rock are the basis of many construction and building materials such as concrete and asphalt in which the aggregates are compounded with a binder. Other construction applications, such as subsurface drainage systems employ unbound aggregates which are poured or mechanically compacted to form rigid structures [1], so-called aggregate packings [2,3]. One specific application of a bound permeable material is porous asphalt concrete. However, due to the relatively low open porosity ε of $0.15 < \varepsilon < 0.25$ and the relatively small size of its pores, porous asphalt for road pavements is prone to clogging [4–6]. Increasing the porosity of asphalt concrete would not only reduce the clogging problem but also enable applications such as energy harvesting from roads. To harvest energy from pavements, one approach proposes to embed air filled tubes into the pavement [7]. With increasing pavement temperature, the air expands and drives a turbine to generate electricity. A positive side effect of this technology is the alleviation of urban heat islands in modern cities, through cooling of the pavement [8–10]. However, introducing tubes into the asphalt pavement complicates the recycling of the pavement material. A pavement material that is highly porous and

permeable to air and water but does not contain foreign objects such as tubes could enable energy harvesting while retaining its recyclability. Another drawback of porous asphalt with conventional aggregates is that the pavement durability decreases with increasing porosity [11]. The durability could potentially be improved by engineered interlocking aggregates that form a rigid yet porous packing.

An associated challenge is the accurate determination of the water permeability of construction materials that are composed of packings of aggregates. Studies correlating the packing porosity and permeability are thus far limited by the narrow range of porosities that can be achieved with conventional aggregates. The earliest method to determine the permeability of an aggregate packing was proposed by Darcy [12] in 1856 by relating the water flux q through a packing with its permeability k and the pressure gradient $\frac{dp}{dx}$ over the packing, viz.:

$$q = -\frac{k}{\nu_w \rho_w} \frac{dp}{dx} \quad (1)$$

where ν_w and ρ_w are the kinematic viscosity and density of water. However, measuring simultaneously the flux and pressure drop can be challenging. For Reynolds numbers (Re) < 1 , an empirical correlation to determine the permeability of a packing based on ε and the aggregate sphericity Ψ and diameter d_p , was proposed by Kozeny in 1927 [13], and later refined by Carman [14,15]:

* Corresponding author.

E-mail address: muelchri@ethz.ch (C.R. Müller).

$$k = \frac{\psi^2 d_p^2 \varepsilon^3}{150(1-\varepsilon)^2} \quad (2)$$

The original equation of Kozeny incorporates tortuosity τ , a parameter that gives the mean path length of a fluid particle when percolating through the packing. In the revised version of Carman, tortuosity is incorporated in the scaling constant (150) using experimental data. To this day, the validity of the Carman-Kozeny correlation (Eq. (2)) has been confirmed by a vast number of studies [16–19]. However, the physical packings studied in these works usually covered only a small range of ε , e.g. for pervious concrete [19] and fiber mats [17] porosities in the range of, respectively, $0.1 < \varepsilon < 0.35$ and $0.5 < \varepsilon < 0.8$ were typically encountered. Other studies have investigated wider ranges of ε , but considered non-physical packings such as randomly placed obstacles [16,20], or fractal geometries [18]. A critical evaluation of the validity of the Carman-Kozeny correlation over a wide range of ε for physical packings is missing thus far.

Above we have outlined two current challenges: (i) the requirement of aggregate packings to accommodate a large porosity to enable novel applications such as energy harvesting from pavements, without reducing their durability, and (ii) the open validation of the Carman-Kozeny correlation for physical packings covering a wide range of ε . Both challenges persist because current methods for aggregate production yield irregularly shaped aggregates, which in the case of crushed rock and gravel are approximately cubical [61]. The use of irregularly, cubically, shaped aggregates, however, limits the range of attainable packing porosities, as cubes form relatively dense packings compared to other shapes [22–24]. Despite the practical importance of aggregates as construction materials, they are commonly used in their “natural state” and their shape is not specifically designed to optimize the aggregate packing for certain properties. Yet, recently a new type of artificial aggregate with engineered shapes, such as stars, tetrapods, and dolosse has been proposed [24–26]. Indeed such shapes have been also used in marine engineering to construct breakwaters, since shapes such as tetrapods and dolosse have been shown to form porous yet stable packings [27]. Advances in 3D printing have unlocked the manufacturing capabilities of such artificial aggregates using polymers [25], or even ceramics [28]. Additionally, aggregate shapes can be designed to be geometrically interlocking, enabling freestanding loadbearing structures of unbound aggregates [26,29–31]. This loadbearing property makes the construction of unbound building facades possible, for example in urban canyons, allowing the porosity to be optimized for noise absorption in addition to the mitigation of heat islands as discussed above [32]. Simultaneously, however, the interlocking property reduces the compactibility and workability of the material, as evidenced by an increase of the shear strength with decreasing aggregate sphericity [33].

Here we investigate artificial aggregates of different shapes and quantify their packing properties such as porosity, tortuosity, and water permeability, and in doing so assess the validity of the Carman-Kozeny correlation for physical packings covering a wide range of porosities for $Re = 0.56$. Packings are constructed both experimentally from model polymer aggregates in an unbound configuration and numerically using the discrete element method (DEM). Subsequently, the permeability is computed numerically using the lattice Boltzmann method (LBM) and validated experimentally using the falling pressure head method.

2. Materials and methods

Fig. 1 gives an overview of the materials and methods employed in this work which are divided into a numerical and experimental part. In the numerical part, the DEM is used to create packings composed of three different types of non-spherical aggregate shapes, viz. tetrapods, dolosse and tetrahedra (see Fig. 2). Since the full 3D geometrical information is known for the packings generated with the DEM,

the porosity of these packings can be determined with high accuracy. Computing the tortuosity requires an intermediate step in which the 3D geometric information is converted into binary data sets, that distinguish between aggregate matter and voids and are stored as images that slice the packing horizontally. To compute the permeability of water in a given numerical packing, the geometrical information is converted into a stereolithographic (STL) file which requires triangular tessellation of the aggregate surfaces. Subsequently, the STL file is used to construct the geometry to compute the permeability via LBM simulations.

In the experimental part of this work, aggregates of two different tetrapod shapes are constructed from acrylonitrile butadiene styrene (ABS) polymer via injection molding. These aggregates are poured into a container to construct packings, which are then used to determine the packing porosity from the weight of water filling the voids. The packings are further used to determine their water permeability via the falling pressure head method. One of the constructed packings, i.e. using tetrapods with sphericity $\Psi = 0.53$, is imaged using X-ray computed tomography (CT) to obtain identical, full 3D geometry information as from the DEM simulations. This experimentally obtained 3D geometry of the packing is used to compute the porosity, tortuosity and permeability of the packing utilizing the same numerical methods as for the DEM packings.

2.1. Numerical materials and methods

2.1.1. Aggregate shapes

The aggregate shapes studied here are constructed by intersecting identical spherocylinders, i.e. cylinders with hemispherically capped ends. In doing so, three different types of artificial aggregate shapes are constructed, viz. tetrapods, dolosse and tetrahedra. The aggregate shapes are visualized in Fig. 2.

A tetrapod is constructed from four spherocylinders, which extend from the center of gravity of a regular tetrahedron to the four vertices of the tetrahedron. The hemispherical endcaps of the spherocylinders in the center of gravity are congruent with a sphere around the center of gravity of the tetrahedron.

Dolosse are constructed by combining three spherocylinders such that they form a H. The base point of each hemispherical endcap of the central spherocylinder lies exactly at the center of the central axis of an outer spherocylinder. To complete a dolos, one of the outer spherocylinders is then rotated by 90° to be perpendicular to the other two spherocylinders.

Tetrahedra are constructed from six spherocylinders each lying on one of the six edges of a tetrahedron. The hemispherical endcaps of the spherocylinders are congruent in the four vertices of the tetrahedron.

For each type of aggregate, a variety of aggregates of varying sphericity (Ψ) are constructed by changing the length and diameter of the constituent spherocylinders. Here the sphericity is defined as the surface area of a sphere with the same volume as the non-spherical aggregate divided by the surface area of the non-spherical aggregate. The reader is referred to the supplemental material (Section A and Fig. S2) for a visualization of the sphericity calculation and additional information. All aggregates considered in this study have the same volume of 733 mm^3 . The diameters and aspect ratios of all of the simulated aggregate shapes can be found in the supplemental material (Section A). An infinite number of aggregate shapes could be constructed by varying the diameters and aspect ratios of the intersecting spherocylinders, which would lead to arbitrarily complex packings. The reason for using identical spherocylinders to construct an aggregate is to reduce complexity. For the same reason, packings are created by using only aggregates of identical type and sphericity.

In addition to sphericity (Ψ), the shape of the aggregates is also described quantitatively by their convexity (Ω). The convexity is defined as the volume of the aggregate divided by the volume of the convex

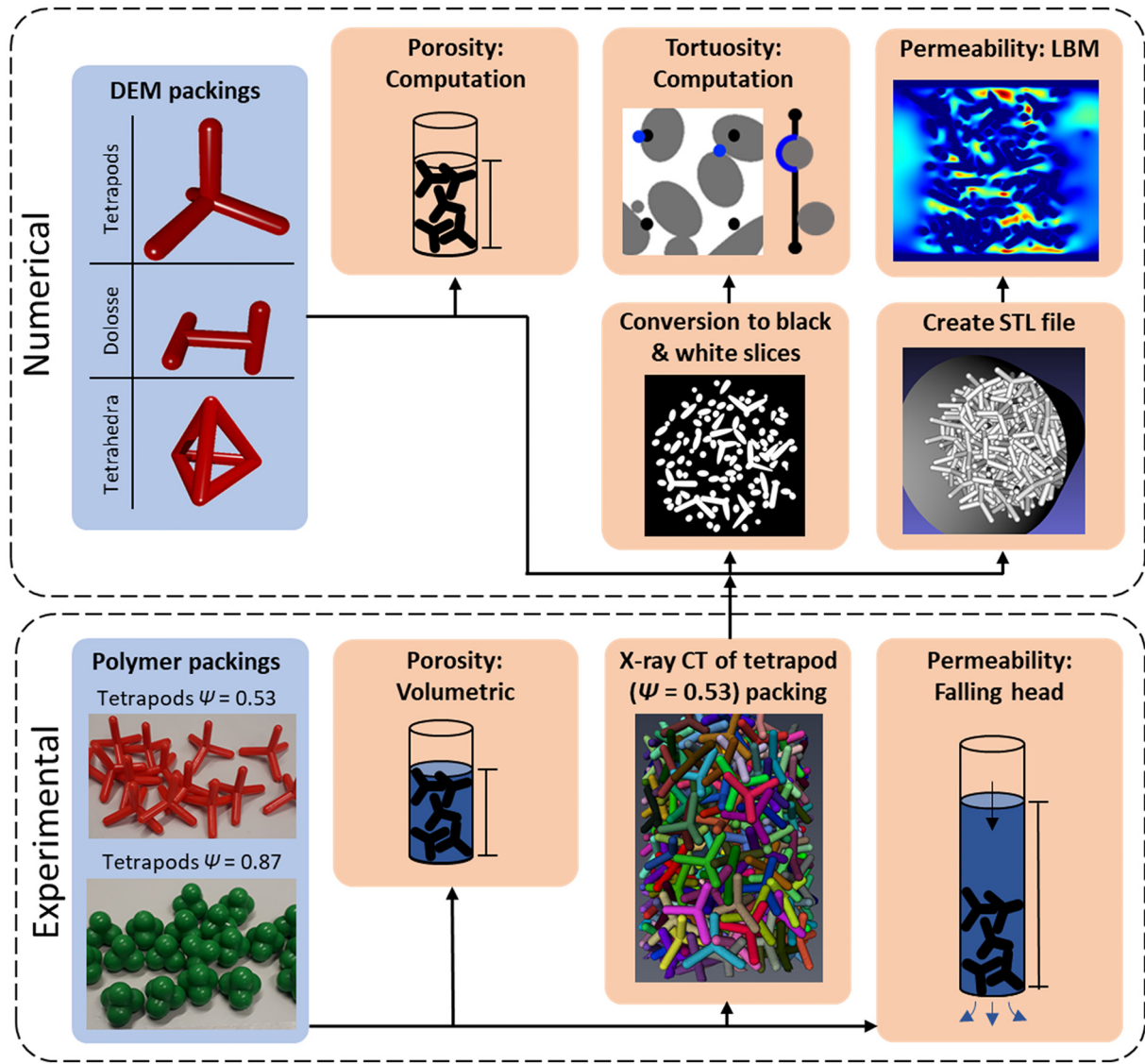


Fig. 1. Overview of the materials and methods applied in the numerical and experimental parts.

hull enveloping the aggregate. A description of the convex hull is given in the supplemental material (Section B and Fig. S3).

2.1.2. Discrete element method (DEM)

The DEM was originally developed by Cundall & Strack [34] for spherical particles, and has been extended to model non-spherical particles [35–38]. In this work, an in-house DEM framework is used which models non-convex aggregates by combining multiple intersecting spherocylinders to form the aggregates shown in Fig. 2.

The DEM treats each aggregate as a discrete element moving freely in space. In the DEM time is advanced by performing the following operations in a timestep: (i) based on the known position of the particles, $x(t)$, determine whether contacts exist, (ii) calculate the contact forces, (iii) determine the acceleration acting on the individual aggregates via Newton's second law of motion and (iv) update the new position of the aggregated, $x(t + \Delta t)$ through Eqs. (3) and (4).

The velocity v_i of an aggregate i at timestep t is calculated through a third-order Adams-Bashforth scheme:

$$v_i(t) = v_i(t - \Delta t) + \frac{\Delta t}{12} [23a_i(t - \Delta t) - 16a_i(t - 2\Delta t) + 5a_i(t - 3\Delta t)] \quad (3)$$

where $a_i(t)$ is the acceleration of aggregate i . The new position x_i of the aggregate is then obtained via:

$$x_i(t) = x_i(t - \Delta t) + \frac{\Delta t}{12} [23v_i(t - \Delta t) - 16v_i(t - 2\Delta t) + 5v_i(t - 3\Delta t)] \quad (4)$$

Modelling non-spherical aggregates requires information on the aggregate orientation, angular velocity $\omega(t)$, and angular momentum $\mathbf{J}(t)$. The angular momentum of aggregate i is found by integrating the net torque M acting on the aggregate:

$$\mathbf{J}_i(t) = \mathbf{J}_i(t - \Delta t) + \frac{\Delta t}{12} [23M_i(t - \Delta t) - 16M_i(t - 2\Delta t) + 5M_i(t - 3\Delta t)] \quad (5)$$

To obtain the angular velocity ω_i the angular momentum is divided by the moment of inertia matrix \mathbf{I} of the aggregate:

$$\omega_i(t) = \frac{\mathbf{J}_i(t)}{\mathbf{I}_i} = \mathbf{J}_i(t) \mathbf{I}_i^{-1} \quad (6)$$

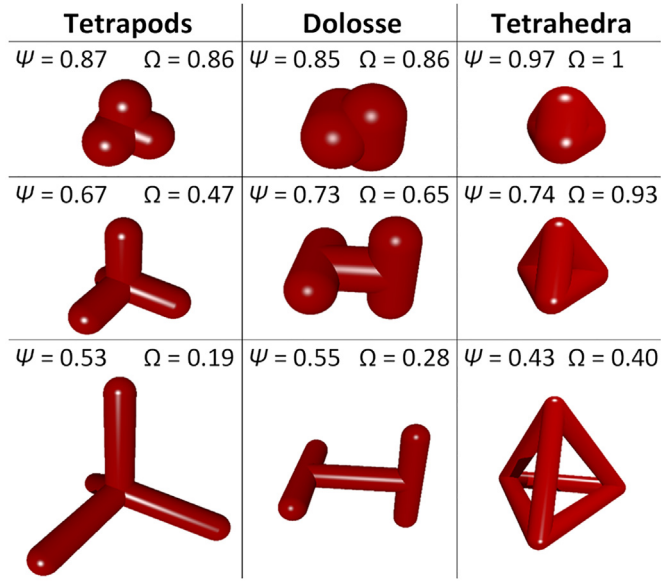


Fig. 2. The different artificial aggregate types and aggregate sphericities that are investigated in this work.

The orientation of the aggregate can be described by a rotation matrix based on Euler angles. However, this rotation matrix has the disadvantage of having singularities. To circumvent this limitation, the DEM commonly employs quaternions [35]. The rotation matrix which describes the aggregate orientation can be calculated from the quaternion q , while the quaternion is calculated for each timestep by integration:

$$\dot{q}_i(t) = \frac{\Delta t}{12} [23\dot{q}_i(t-\Delta t) - 16\dot{q}_i(t-2\Delta t) + 5\dot{q}_i(t-3\Delta t)] \quad (7)$$

with

$$\begin{bmatrix} \dot{q}_{i,1}(t) \\ \dot{q}_{i,2}(t) \\ \dot{q}_{i,3}(t) \\ \dot{q}_{i,4}(t) \end{bmatrix} = \frac{1}{2} \begin{bmatrix} q_{i,1}(t) & -q_{i,2}(t) & -q_{i,3}(t) & -q_{i,4}(t) \\ q_{i,2}(t) & q_{i,1}(t) & -q_{i,4}(t) & q_{i,3}(t) \\ q_{i,3}(t) & q_{i,4}(t) & q_{i,1}(t) & -q_{i,2}(t) \\ q_{i,4}(t) & -q_{i,3}(t) & q_{i,2}(t) & q_{i,1}(t) \end{bmatrix} \begin{bmatrix} 0 \\ \omega_{ix}(t) \\ \omega_{iy}(t) \\ \omega_{iz}(t) \end{bmatrix} \quad (8)$$

Once the new positions, orientations, and (angular) velocities of all aggregates have been updated a new contact search starts.

Detecting contacts between spherocylinders requires the calculation of the distance between the central axes of neighboring spherocylinder (shown in red in Fig. 3). If the distance between the central axes of two spherocylinders is smaller than two times the spherocylinder radius r the aggregates are in contact. In the present DEM framework, finding the distance between two line segments (i.e. central axes) is solved using the algorithm proposed by Lumelsky [39]. The contact point between two spherocylinders is the middle point of the shortest line between the central axes of two contacting spherocylinders (see green line in Fig. 3a). The

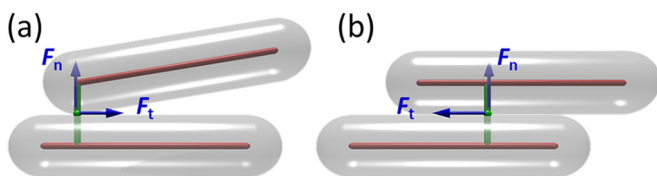


Fig. 3. Sketch depicting two contacting spherocylinders. (a) Oblique contact. (b) Parallel contact.

contact forces (blue arrows in Fig. 3) act at the contact point between two spherocylinders. If the central axes of two contacting spherocylinders share a parallel segment, as seen in Fig. 3b, there is no single shortest line between the two central axes. In this case the contact point is the middle point of the line which is in the center of the parallel segment.

The contact force acting at the contact point can be decomposed into a normal contact force F_n and, assuming a non-zero friction coefficient, a tangential contact force F_t . Both contact forces are modelled by a linear spring dashpot which yields a constant coefficient of restitution. The contact force in the normal direction between aggregate i and j is given as:

$$F_n = \max \left(0, \frac{s_n}{2} \delta_n - \eta_n \sqrt{2m_{ij}s_n v_n} \right) \quad (9)$$

where s_n is the normal stiffness of the aggregate, δ_n is the overlap between the contacting spherocylinders, η_n is the normal damping factor, v_n is the normal component of the relative velocity between the aggregates at the contact point and m_{ij} is the effective inertial mass of aggregates i and j which is given by:

$$m_{ij} = \frac{m_i m_j}{m_i + m_j} \quad (10)$$

In the tangential direction the contact force is modelled following Coulomb's law of friction:

$$F_t = \min \left(\mu \frac{s_n}{2} \delta_n, \frac{s_t}{2} \delta_t - \eta_t \sqrt{2m_{ij}s_t v_t} \right) \quad (11)$$

where μ is the coefficient of friction, η_t is the tangential damping factor, s_t is the tangential stiffness and v_t is the tangential component of the relative velocity between the aggregates at the point of contact. The accumulated tangential displacement at the contact point is calculated as $\delta_t = \int v_t dt$.

Once all contact forces acting on a given aggregate i have been calculated they are summed up and the resulting force $F_{sum,i}$ allows to calculate the acceleration acting on aggregate i :

$$a_i(t + \Delta t) = \frac{F_{sum,i}}{m_i} \quad (12)$$

For non-spherical aggregates contact forces also induce a torque M_i :

$$M_i(t + \Delta t) = \sum_c r_c \times (F_{n,c} + F_{t,c}) \quad (13)$$

where the index c loops over all contacts of aggregate i and r_c is the vector pointing from the center of gravity of the aggregate to the contact point.

The values of the parameters used in the DEM simulations were chosen to model the properties of ABS aggregates [40]. The parameters are listed in Table 1. It is worth noting that the DEM values chosen to describe the stiffness of the aggregates are commonly much lower than the physical values to allow for larger time steps

Table 1
Parameters used for DEM simulations.

Parameter	Symbol	Value
Density	ρ	1000 kg/m ³
Normal stiffness	s_n	10'000 N/m
Tangential stiffness	s_t	5'000 N/m
Coefficient of restitution	e	0.3
Normal damping factor	η_n	0.35
Tangential damping factor	η_t	0.3
Coefficient of friction	μ	0.35
Wall friction coefficient	μ_w	0.1
Time step	Δt	10 ⁻⁵ s

as the time step size is typically ~ 20 times the collision time t_{col} which is given by [41]:

$$t_{col} = \frac{\pi}{\sqrt{\frac{S_n}{m_{ij}} (1 - \eta_m^2)}} \quad (14)$$

In the present work, as it has been shown that the magnitude of the stiffness has negligible effects on the packing properties, a value of 10,000 N/m was chosen for the normal stiffness, which allows for a Δt of 10^{-5} s, [42]. The value for the tangential stiffness was chosen as half the normal stiffness in accordance with previous studies [31,36,43].

All aggregate packings are modelled in a cylindrical simulation domain with a diameter of 100 mm and a height of 700 mm, which matches the acrylic cylinder used for the physical experiments. The DEM domain is filled by creating aggregates at a height of 600 mm in batches of 3 by 3 aggregates. Between each aggregate, there is a gap of the same size as the diameter of the constituent spherocylinders of the aggregate. Additionally, each aggregate is given a random orientation and a random initial velocity in both horizontal directions of v_{ini} ($-0.5 \text{ m/s} < v_{ini} < 0.5 \text{ m/s}$). Immediately upon their creation, the aggregates fall to the bottom of the cylinder domain and after 0.11 s a new 3 by 3 batch of aggregates is created. This step is repeated until a sufficient number of aggregates has been created to yield a packing height of at least 350 mm. The number of aggregates used to model each packing is given in the supplemental material (Section A). Once all aggregates are created, the packing obtains its equilibrium position within 1 s and the simulation is stopped.

The DEM data is exported as a stack of black and white (binary) images that represent horizontal slices through the packing. These slices are rendered using the ray tracing software POV-Ray [44]. An extended description of the rendering of the slices is given in the supplemental material (Section C). The porosity ε of the DEM packings is determined by:

$$\varepsilon = \frac{1 - V_{agg}}{V_{domain}} \quad (15)$$

where V_{agg} is the total volume of all aggregates and V_{domain} is the volume of the cylindrical domain, i.e. from the bottom to the highest point of the aggregate packing. For each type of aggregate, a fourth-order polynomial was fitted to the ε versus Ψ data points to yield an ε - Ψ relationship which can be used to evaluate the Carman-Kozeny equation. To construct the fluid domain for the LBM simulations, the geometrical information of the DEM packings is converted into STL files. An explanation of this conversion process is given in the supplemental material (Section D).

2.1.3. Computing the tortuosity of a packing

The tortuosity is defined as the length of the shortest path through the pore space of a packing divided by the length of a straight line through the packing. In the present work the goal is to compute the tortuosity solely based on geometric information of the packing, i.e. the so-called geometric tortuosity [45]. Alternative methods to calculate the tortuosity, e.g. the hydraulic tortuosity which can be computed e.g. through the method proposed by Duda et al. [46], require also information on the fluid velocity in the porous medium. A separate investigation described in section E of the supplemental material shows that the method by Duda et al. [46] is a less suitable measure of the tortuosity of pavements constructed of artificial aggregates compared to the geometric tortuosity. Hence, a method to calculate the geometric tortuosity of packings was developed in this work. This method relies on the binary horizontal slices through the packing. Neighboring slices have a vertical separation of 0.2 mm. For all DEM packings investigated, the top and bottom 30 mm are ignored for the tortuosity analysis due to wall and free-surface effects.

The tortuosity calculation starts with the top slice of the central section of the packing. A grid of dots spaced 5 mm is drawn on this slice, see black dots in Fig. 4. These black dots are drawn in the same positions on all slices. If a black dot lies inside an aggregate, the closest point not lying inside the aggregate is found (blue dots in Fig. 4). For each blue dot a line is drawn connecting the blue dot and the associated black dot. The following restriction for finding the blue dots is applied: If the angle between the two lines connecting the black dot with its associated blue dots on two subsequent slices is larger than 45° the blue dot on the second slice is rejected. Instead, a new blue dot is found which is closest to the center of the line connecting the black dot and the blue dot on the first of the two neighboring slices. This scheme is illustrated in Fig. 4a where one of the black dots has been highlighted in yellow. The closest surface point to the yellow dot in the first slice, Fig. 4a, is the red dot. In the following slice, Fig. 4b, the closest surface point to the yellow dot is the green dot. The red dot from slice 4a is superimposed on the slice in Fig. 4b for demonstration. Since the angle between the line connecting the red and yellow dots and the line connecting the green and yellow dots is larger than 45° , the green dot will be rejected. Instead, a new closest surface point (purple dot) is found for the center of the line connecting the red and yellow dots. In the aggregate packings investigated here less than 0.01% of the dots were rejected. Furthermore, varying the rejection angle between 0° and 90° has no measurable effect on the calculated tortuosity values. However, changing the vertical resolution, i.e. the distance between slices could affect the determined tortuosity values.

Once all slices have been processed, a tortuous path through the packing is obtained by connecting each black dot with the corresponding black dot on the subsequent slice or with the corresponding closest blue dot if the black dot lies inside an aggregate. Such a tortuous path is sketched in Fig. 4c. The tortuosity of one path is calculated by dividing the length of the path by the length of a straight line connecting the start and end of the path. To calculate the tortuosity of an entire packing the tortuosity of all paths for the given packing is averaged. Typically, 208 paths per packing are calculated. When varying the number of

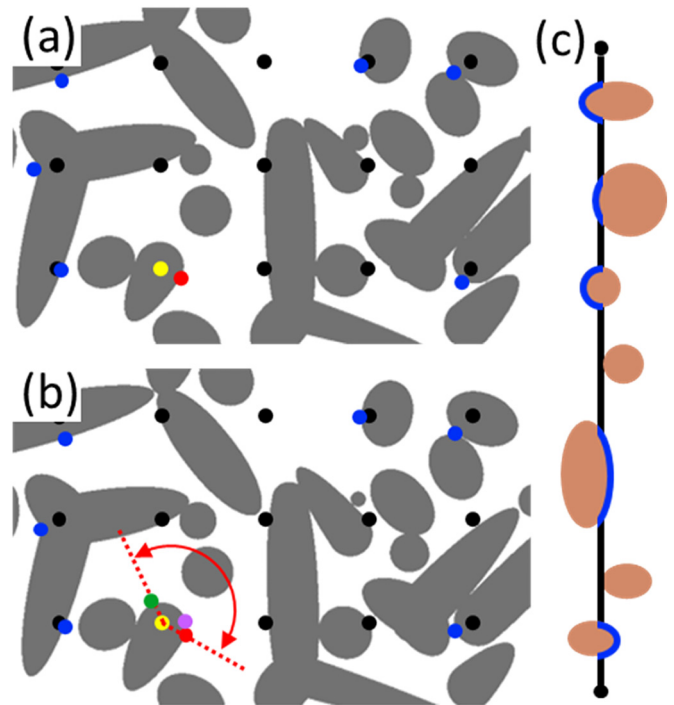


Fig. 4. (a) Horizontal slice through a packing of tetrapods with $\Psi = 0.53$. (b) Horizontal slice that is located 0.2 mm below the slice shown in (a). (c) Illustration of the construction of a tortuous path through the packing.

paths from 80 to 3500 the computed tortuosity values fluctuate by only $\pm 2\%$.

2.1.4. Lattice Boltzmann method (LBM)

Owing to its high versatility for complex boundary systems, the LBM method is used to calculate the flow field in the aggregate packings. Here we use the open source LBM framework Palabos [45]. To this end the STL files are imported and the surface of the aggregates is modelled by bounce-back walls. At the inlet a Poiseuille flow profile is prescribed with an average velocity $u = 0.05$ mm/s. This ensures a low Reynolds number laminar flow. Unfortunately, high Reynolds number flows, as encountered in the falling head experiments, cannot be modelled due to stability limitations of the LBM approach. Nonetheless, it is possible to compare the results of the falling head experiments and the simulations, provided that the experiments are evaluated with the Darcy-Forchheimer equation that is appropriate for turbulent flows (Eq. (18)), while the simulations are evaluated with the Darcy equation for laminar flows (Eq. (17)). An additional investigation, detailed in section F of the supplemental material, revealed that the permeability values obtained through LBM simulations do not vary with the Reynolds number.

The outlet is modelled with a Neumann boundary condition, i.e. a zero-velocity gradient and a constant pressure equal to the ambient pressure. The modelled fluid is water with a density (ρ_w) of 1000 kg/m³ and a kinematic viscosity (ν_w) of 10^{-6} m²/s. The LBM solver uses the incompressible Bhatnagar-Gross-Krook (BGK) model [46]. The non-dimensional lattice viscosity ν_{lat} is varied between 0.01 and 0.05 to yield optimal convergence. The time step size dt and the lattice viscosity are related through:

$$dt = \frac{\nu_{lat}}{\nu_w dx^2} \quad (16)$$

where dx is the lattice spacing. The fluid space is discretized using a D3Q19 lattice with equally spaced nodes in all three directions, i.e. $dx = dy = dz = 133.33$ μ m, yielding up to 540 million nodes per simulation, with computations running on 420 CPU cores for approximately 12 h.

Once the LBM simulations have reached a steady state, the permeability k is determined by applying Darcy's law:

$$k = \frac{L \nu_w \rho_w u}{\Delta P} \quad (17)$$

where L is the height of the packing and ΔP is the pressure drop between the inlet and outlet.

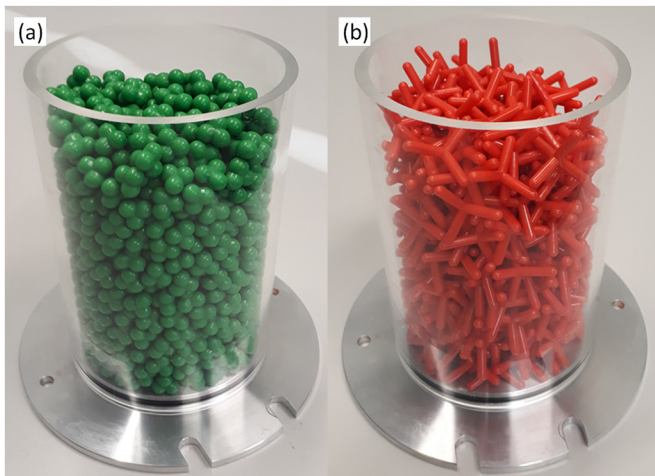


Fig. 5. Physical tetrapods of different sphericities packed into an acrylic pipe with 100 mm diameter, the sphericities of the tetrapods are: (a) $\Psi = 0.87$ and (b) $\Psi = 0.53$.

2.2. Experimental materials and methods

2.2.1. Polymer aggregates

To verify the numerical results experimentally, physical tetrapods of two different sphericities ($\Psi = 0.87$ and $\Psi = 0.53$) are used. These physical aggregates are manufactured from an ABS polymer via injection molding with identical geometries as the numerical aggregates. Images of the physical aggregates can be found in Fig. 5. These two tetrapod shapes are chosen to cover the wide range of tetrapod sphericities that were investigated numerically ($0.99 \geq \Psi \geq 0.47$). Since initial comparisons of the experimentally and numerically determined porosity showed good agreement it was deemed unnecessary to manufacture additional shapes for validation.

2.2.2. Volumetric porosity determination

To create the packings, the injection molded aggregates are poured into an acrylic cylinder of inner diameter 100 mm and a height of 140 mm. While pouring, it is ensured that the resulting packing is random, for example by not vibrating the packing, which could reduce randomness by aligning aggregates and potentially increasing the packings load-bearing capacity. Ensuring randomness can lead to large voids in packings of low sphericity (e.g. tetrapods with $\Psi = 0.53$), due to arching of the aggregates. Such large voids are tolerated and are considered part of the statistical variations in the packings. The porosity of these packings is measured by filling the interstitial void space between the aggregates with water such that the aggregates are fully submerged. The porosity is given by the weight of the water divided by the density of water and the volume of the pipe containing the aggregates. Since the aggregates are buoyant in water the packing is weighed down by a wire mesh placed on top.

2.2.3. Permeability using the falling head method

The permeability of the packings is determined using the so-called falling head method, a schematic of the experimental setup is shown in Fig. 6. An acrylic cylinder with 100 mm inner diameter and a height of 1.8 m is covered at the bottom with a wire mesh with a mesh size of 8 mm. Aggregates are poured onto this wire mesh to create a packing with a height of 120 mm. For aggregates that are small enough to fall

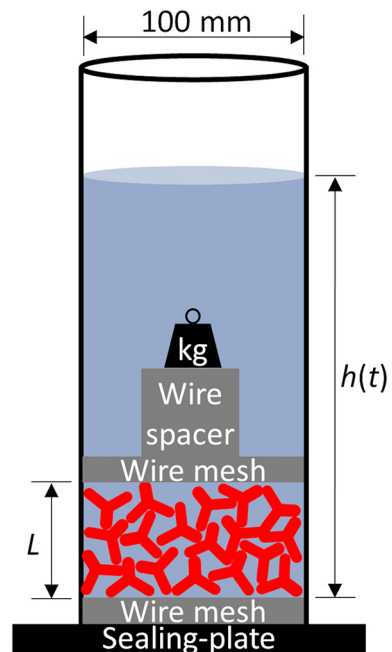


Fig. 6. Schematic of the setup for the falling head experiments.

through this wire mesh a second layer of wire mesh is added, rotated by 45°. The packing is kept in place against buoyance by a weighted wire mesh placed on top, which also prevents a rearrangement of the aggregates due to turbulences during an experiment. For a typical experiment a plate is pushed against the bottom of the cylinder to seal it, and the cylinder is filled with water to a height of 1.6 m above the sample. While filling the cylinder it was ensured that the water jet does not impinge on the packing, to prevent any disturbance of the packing. If a rearrangement of the aggregates is observed while filling the cylinder with water or during an experiment, the experiment is repeated with a freshly prepared packing. An experiment is started by removing the sealing-plate abruptly. The water level is recorded using a Canon EOS 77D camera at 50 frames per second. For the evaluation of the permeability the water level decrease from 1.6 m to 1.3 m is disregarded to ensure the water column is not subject to inertial effects. The recording is stopped once the water level drops to 0.1 m above the packing sample. Hence, the water level from 1.3 m to 0.1 m above the sample is used to determine the permeability of the packing.

A second order polynomial is fitted to the water level, $h(t)$, versus time data, resulting in a smooth curve for $h(t)$ which aids in determining the permeability of the packing via the Darcy-Forchheimer equation for turbulent flows through porous media, viz.

$$-\frac{dp}{dx} = -\frac{\rho_w g(h(t) + L)}{L} = \frac{\nu_w \rho_w}{k} \frac{dh}{dt} + \frac{\rho_w}{k_{in}} \left| \frac{dh}{dt} \right| \frac{dh}{dt} \quad (18)$$

Here, $\frac{\partial p}{\partial x}$ is the pressure drop across the height of the sample L which is equal to the hydrostatic pressure of the water column, ρ_w is the density of water, ν_w is the kinematic viscosity of water and g is the acceleration due to gravity. As the experiments are performed at room temperature the values at 20 °C are used for ρ_w and ν_w , varying these values between 5 °C and 40 °C has negligible effects on the results. Using the Darcy-Forchheimer equation (Eq. (18)) for turbulent flow instead of the Darcy equation (Eq. (17)) for laminar flow ($Re < 1$) is necessary since high flow velocities with $Re > 9000$ are observed in the experiments. The two unknowns to be determined in Eq. (18) are k , i.e. the permeability of the aggregate packing, and the so-called inertial permeability k_{in} . The inertial permeability captures the pressure loss due to turbulence in the flow through the packing. To determine k and k_{in} , Eq. (18) is evaluated at two different times allowing to solve the following system of linear equations

$$\begin{bmatrix} \nu_w \rho_w \frac{d}{dt} h(t_1) & \rho_w \left| \frac{d}{dt} h(t_1) \right| \frac{d}{dt} h(t_1) \\ \nu_w \rho_w \frac{d}{dt} h(t_2) & \rho_w \left| \frac{d}{dt} h(t_2) \right| \frac{d}{dt} h(t_2) \end{bmatrix} \begin{bmatrix} \frac{1}{k} \\ \frac{1}{k_{in}} \end{bmatrix} = \begin{bmatrix} -\frac{\rho_w g(h(t_1) + L)}{L} \\ -\frac{\rho_w g(h(t_2) + L)}{L} \end{bmatrix} \quad (19)$$

yielding in turn k and k_{in} that, however, vary to some extent with $h(t)$. Since k and k_{in} are constants describing the aggregate packing and hence ought to be independent of $h(t)$ the following procedure was applied. First an average value of k_{in} is calculated using the initially obtained values, yielding an almost constant value of k when reevaluating Eq. (19) with a fixed k_{in} . In a second step, the values of k are averaged over time. Additional information on the fitting procedure used to calculate the final values of k is found in section G of the supplemental material. In total six different aggregate packings were investigated, i.e. three packings using tetrapods of $\Psi = 0.87$ and three packings of tetrapods of $\Psi = 0.53$. For each of these packings three $h(t)$ -curves were recorded.

2.2.4. X-ray computed tomography

The full, 3D structure of the physical packings of tetrapods with $\Psi = 0.53$ (see Fig. 2 and Fig. 5b) is recorded using X-ray computed tomography (CT). Due to the effort required to prepare a CT it was decided not to image also the second experimental tetrapod type ($\Psi = 0.87$).

A packing of height 400 mm was poured into an acrylic cylinder (100 mm inner diameter), ensuring randomness and making this packing equal to the experimental packings used for the porosity and permeability investigations. The different height of the packing used for CT and other experimental packings does not affect the packing structure, which was confirmed by numerical simulations. From the packing of 400 mm height a central section of 150 mm height (120 mm diameter) was recorded. The height of this central section is limited by the field of view of the X-ray setup. The X-ray CT setup consisted of an X-ray source (Viscom XT9160) operated at 70 kV and 140 μ A, a digital detector with 2048×2048 pixels (XRD 1621 CN3 ES, Perkin Elmer) and a CsI(Tl) scintillator yielding a high spatial resolution of $66.41 \times 66.41 \times 66.41 \mu\text{m}^3$ per voxel.

The CT data is post-processed in multiple steps using the software Avizo v9.7 (Thermo Fisher Scientific). In the first step the grayscale data is thresholded to separate voxels that contain polymer aggregates from the voxels containing air. The thresholding value was found to have a negligible influence on the total aggregate volume in the CT data due to the large difference in the X-ray absorption between the ABS polymer and air, consequently a thresholding value of 0.2 was chosen (on a range from 0 to 1). The injection molding process produces holes within the aggregates that arise when ABS shrinks during cooling. In a post-processing step these holes are filled digitally such that they do not contribute to the porosity of the packings. Subsequently, a watershed algorithm is used to identify the individual aggregates in the CT data. At the top and bottom of the recorded 150 mm high section some aggregates are incomplete as they are not fully inside the imaged section. Digital sieving is used to remove incomplete aggregates such that only complete aggregates are used for further analysis.

To be able to use the CT data for LBM simulations the post-processed data is exported as a stereolithography (STL) file using Avizo. The STL file describes the surface of the aggregates through triangular facets. The CT data is also exported as a stack of binary images that represent horizontal slices (thickness 0.2 mm) through the packing. These binary images allow to distinguish pixels that are aggregate matter or void. An example of such a binary slice is shown in the supplemental material (- Section C, Fig. S4b).

3. Results and discussion

3.1. Convexity

Fig. 7 plots the convexity (Ω) as a function of sphericity. For all three aggregate shapes studied here, Ω decreases monotonically with decreasing Ψ . For tetrapods and dolosse the slope of the Ω - Ψ -curves increases

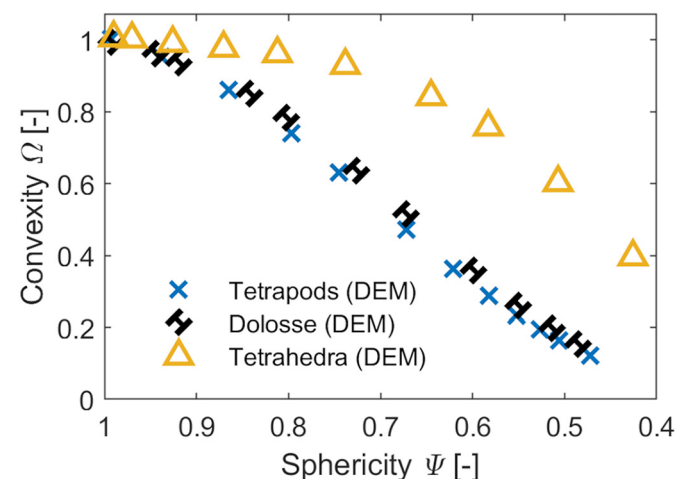


Fig. 7. Convexity of the aggregates studied here as function of the sphericity.

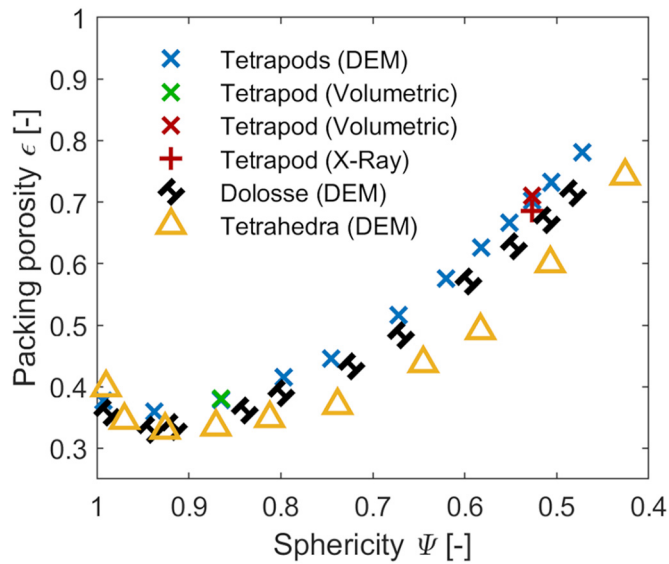


Fig. 8. Packing porosity ε as a function of the sphericity of the packing-forming aggregates Ψ . Each packing was constructed of aggregates of a single shape.

for $\Psi < 0.85$. The reason for this change in slope is that for $\Psi > 0.85$ the cylindrical section of one (or more) of the constituent spherocylinders is completely or partially concealed. This can be seen for example in Fig. 2 for dolosse with $\Psi = 0.85$. Here the central spherocylinder is completely concealed by the two outer spherocylinders. If the sphericity is decreased, e.g. dolosse with $\Psi = 0.73$ (Fig. 2), the third (central) spherocylinder becomes exposed, leading to an increasing reduction in Ω with decreasing Ψ . For tetrahedra there is a change in the slope of the Ω - Ψ -curve for $\Psi < 0.7$. The reason is similar as discussed for the other two shapes, i.e. for tetrahedra with $\Psi > 0.7$ parts of the cylindrical surface of the constituent spherocylinders are concealed in the core of the aggregate. For $\Psi < 0.7$ the core of the aggregate is exposed fully to the outside and the previously concealed cylindrical surface sections contribute to the surface area of the aggregate, hence decreasing Ω .

3.2. Porosity

Combining Darcy's law, Eq. (1), with the Carman-Kozeny equation, Eq. (2), predicts that the permeability of a packing increases with increasing aggregate sphericity Ψ and increasing packing porosity ε .

Fig. 8 plots the porosity of a packing as a function of the sphericity of the packing-forming aggregates. The data in Fig. 8 contains both porosity data from DEM simulations and porosity data obtained experimentally by either volumetric methods or the analysis of X-ray CT data. Comparing the numerical DEM data of tetrapods (blue crosses) with the results of the experimental packing of tetrapods (green and red crosses) shows excellent agreement, confirming that DEM is a viable numerical approach to investigate packings of complex-shaped aggregates. The excellent agreement also shows, that despite differences in the experimental and numerical pouring protocol, similar packings are created, because both pouring protocols ensure a high degree of randomness. The experimental tetrapod ($\Psi = 0.53$) packing with an X-ray CT determined porosity (red plus) of $\varepsilon = 0.685$ is lower than the porosity derived by DEM ($\varepsilon = 0.7$). This is due to the fact that the CT shows a denser-packed central section of the sample, while the DEM packing also includes aggregates in the porosity determination that are located at the bottom of the packing where the porosity is higher due to wall effects. Further evidence for the predictive nature of the DEM simulations is provided by the porosities determined for packings of almost spherical aggregates ($\Psi = 0.99$) which lie in the

range $0.368 < \varepsilon < 0.399$. These porosity values are close to the established value for a random packing of spheres of $\varepsilon = 0.366$ [47].

It is worthwhile to mention that for all three aggregate types there is a minimum in the packing porosity for $\Psi \approx 0.92$. Such a minimum in the porosity of packings that are composed of slightly non-spherical shapes, i.e. $0.99 > \Psi > 0.9$, is well established and has also been reported for other particle types such as ellipsoids or spherocylinders [48–51]. Generally, for $\Psi < 0.92$, the porosity of a packing increases with decreasing sphericity. While the behavior of tetrapods and dolosse overlaps, the porosity of packings of tetrahedra increases to a lesser extent with decreasing sphericity. This finding shows that for non-spherical particles, the sphericity of an aggregate is not the only parameter affecting the porosity of a packing [52]. This observation is re-affirmed by Fig. 7 which shows that the convexity of tetrahedra can differ from the convexity of tetrapods by up to 0.47 for an equal sphericity. Nevertheless for $\Psi < 0.92$ the monotonic increase of packing porosity with decreasing sphericity holds for all aggregate shapes and shows that it is possible to construct packings of very high porosity when using aggregates of low sphericity, e.g. tetrapods with $\Psi = 0.47$ have $\varepsilon = 0.78$. Packings with such high porosities have the potential to enable novel applications such as energy harvesting from recyclable pavements. However, with regards to novel applications it has to be considered that variations in the sphericity of the aggregates also affects the structural properties of the aggregate packing such as stress distribution [31]. To be able to withstand the high inter-particle stresses found in packings of low sphericity aggregates requires material with sufficient mechanical strength. Due to their convex shape, tetrahedra can withstand higher compressive loads compared to non-convex shapes such as tetrapods. However, one needs to consider that tetrahedra with $\Psi < 0.5$ become very slender such that their corners can penetrate into the core of other contacting tetrahedra which would lead to interlocking and hence reduce the workability of the packing. Conversely, if a packing is required that can interlock, e.g. for freestanding structures, shapes such as tetrapods or dolosse that have a lower convexity compared to tetrahedra are beneficial, as it has been shown that packings of aggregates with lower convexity sustain higher shear stresses [53].

In the following we will utilize the observation that by varying aggregate sphericity, packings with a wide range of porosities can be constructed to assess the validity of the Carman-Kozeny correlation for differently shaped aggregates and a wide range of packing porosities.

3.3. Tortuosity

Fig. 8 has demonstrated that the packing porosity depends on the aggregate sphericity Ψ , as well as the aggregate convexity, and that aggregates of different shapes but similar sphericity do not necessarily form packings with the same porosity. However, there is a second question to be addressed: Do packings of aggregates of different shapes but similar sphericity form pore spaces of similar morphology? Answering this question requires a descriptor for the morphology of the pore space. In the following we will use the tortuosity τ as a descriptor for morphology of the pore space. Fig. 9a plots the variation of τ with aggregate sphericity Ψ for the three different aggregate shapes studied, we observe a convex-shaped trend of τ with Ψ with a maximum in τ at $\Psi \approx 0.92$ for tetrapods and dolosse. The overall behavior of tetrahedra is similar with a maximum in τ located at $\Psi = 0.81$.

For tetrapods and dolosse the relationship between τ and Ψ (Fig. 9a) shows a similar trend as the relationship between ε and Ψ (Fig. 8), albeit mirrored along the Ψ axis. Both ε and τ have an extremum at $\Psi \approx 0.92$. The tortuosity of the tetrapod packing ($\Psi = 0.53$) as determined by X-ray CT is $\tau = 1.61$, agrees well with the DEM derived tortuosity of the same packing which is $\tau = 1.58$. The fact that for packings of tetrapods and dolosse of low Ψ we obtain high values of ε and low values of τ would suggest that these packings would feature a high permeability.

Packings of tetrahedra show some differences to the tortuosity of packings of tetrapods and dolosse, viz. the tortuosity of packings of

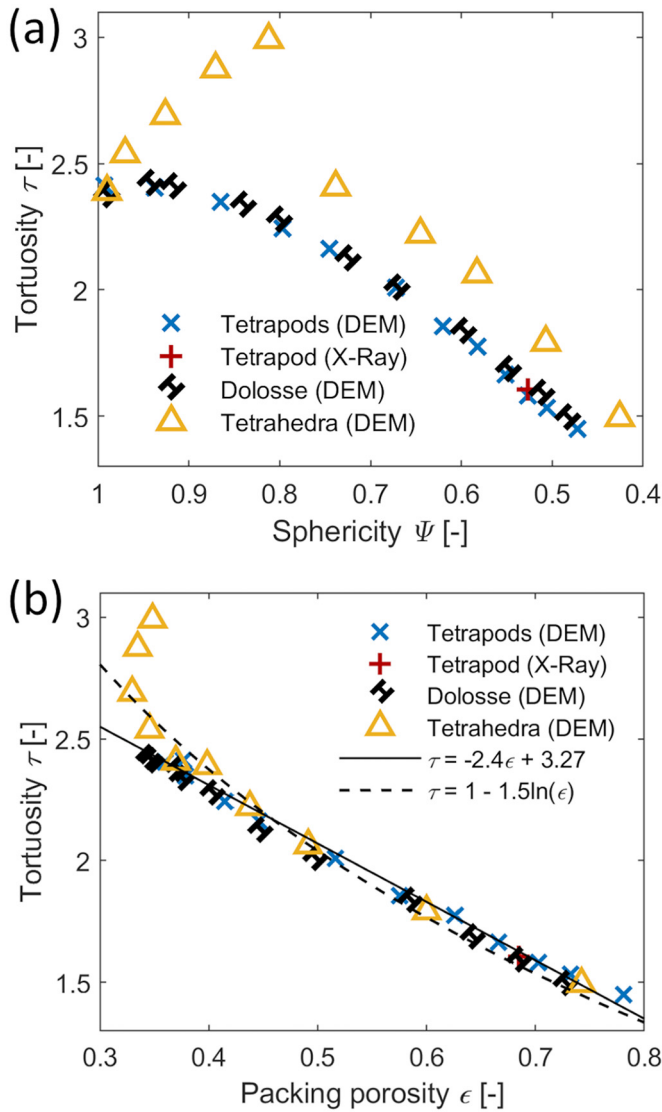


Fig. 9. (a) Tortuosity of a packing as a function of the sphericity of an aggregate Ψ . (b) Tortuosity of a packing as a function of the packing porosity ϵ .

tetrahedra increases for $\Psi > 0.81$ with increasing Ψ , but drops sharply to $\tau = 2.4$ at $\Psi = 0.74$. The reason for this drop is that at $\Psi = 0.81$ the inside space of the tetrahedron is closed and inaccessible from the outside, similar to the example shown for $\Psi = 0.97$ in Fig. 2. The shortest path through a packing is a curve around the (outer) surface of the entire tetrahedron, leading to a long path length. Additionally, closed tetrahedra tend to align face to face leaving no void space between the aggregates, increasing the path length further. However, for $\Psi \leq 0.74$ tetrahedra have an open structure, e.g. as shown for $\Psi = 0.43$ in Fig. 2. For such an open tetrahedron the inside of the aggregate becomes accessible, offering a shortcut through the aggregate resulting in turn in a shorter path through a packing. For $\Psi < 0.74$, τ decreases with decreasing sphericity in a similar fashion as for tetrapods and dolosse, yet for a given sphericity, the value of τ for packings of tetrahedra is higher than for tetrapods and dolosse. The results above show that aggregates of different shapes but similar sphericity do not necessarily form packings of similar pore space morphology. However, for all particle shapes we find overall similar trends between τ and Ψ and between ϵ and Ψ which hint towards a correlation between τ and ϵ .

Fig. 9b shows that there is a linear correlation between τ and ϵ for $\epsilon > 0.35$ that can be approximated by:

$$\tau = -2.4\epsilon + 3.27 \quad (20)$$

If this linear correlation is extended to higher values of ϵ , it gives $\tau \rightarrow 1$ for $\epsilon \rightarrow 1$. Indeed, a value of $\tau = 1$ at $\epsilon = 1$ is expected since a tortuous path through a volume without any aggregates is a simple straight path. However, for $\epsilon < 0.35$ we observe a non-linear increase of τ with decreasing porosity for packings of tetrahedra. Packings with such high tortuosity values (i.e. $\tau > 2.5$) correspond to the previously discussed packings of closed tetrahedra which align face to face.

In the past, a large number of correlations relating τ to ϵ have been proposed [54–56]. However, similar to the Carman-Kozeny correlation, these functions have typically not been tested for porous structures covering a wide range of values for ϵ , but rather packings of very specific particle shapes such as spherical packings ranging from the random-close to random-loose packing limit ($\epsilon = 0.366$ – 0.46) [57] or random packings of fibres ($\epsilon = 0.9$ – 0.96) [58]. In other works the τ - ϵ correlations have been tested over a wider range of values for ϵ , but for artificial structures such as fractals or randomly placed obstacles [59,60]. Thus, in the following, the packings of aggregates model by DEM, which cover a wide range of porosity values and that have been validated by physical experiments, are used to establish a τ - ϵ relationship, viz.:

$$\tau = 1 - p \ln(\epsilon) \text{ with } p = 1.5 \quad (21)$$

Eq. (21) has been suggested in the literature (e.g. [60]) and the coefficient $p = 1.5$ has been found to give the best fit to the data shown in Fig. 9b. However, it is worth noting that Eq. (21) cannot capture the non-linear behavior of tetrahedra for $\tau > 2.5$. The reason is that Eq. (21), as most other τ - ϵ correlations, is developed for random isotropic porous structures. As tetrahedra tend to align face to face (and with the walls) for $0.97 \geq \Psi \geq 0.81$ ($\epsilon < 0.35$) such packings cannot be considered fully random.

The linear correlation between τ and ϵ (when excluding particular aggregate structures), indicates that tortuosity might not be required as an additional parameter to determine the permeability of a packing, instead tortuosity can be capture by porosity through a scaling factor.

3.4. Permeability

Fig. 8 has shown that the packing porosity increases with decreasing particle sphericity (for $\Psi < 0.92$); similarly, also the packing tortuosity decreases with decreasing permeability (Fig. 9), except for tetrahedra for $\epsilon < 0.35$. Both findings suggest that the packing permeability increases with decreasing particle sphericity. To test this hypothesis and to test the validity of the Carman-Kozeny correlation for packings of complex-shaped aggregates, the permeability of packings was investigated numerically via LBM simulations and experimentally using the falling head method. Fig. 10a plots numerically and experimentally determined permeabilities k as a function of the particle sphericity Ψ .

The k - Ψ data plotted in Fig. 10a show a similar trend as the ϵ - Ψ data given in Fig. 8, i.e. also the permeability has a minimum at $\Psi \approx 0.9$ and for $\Psi < 0.9$ the permeability increases monotonically with decreasing Ψ . Note that the k - Ψ data is plotted, as it is typically done, on a semilogarithmic scale. The strong similarity of the k - Ψ and ϵ - Ψ trends suggest a direct correlation between k and ϵ (see below). When comparing the numerically determined permeabilities with the predictions of the Carman-Kozeny correlation (Eq. (2)) a good agreement is obtained. Since the Carman-Kozeny correlation only depends on Ψ , ϵ and the (equivalent) aggregate diameter, this indicates that the tortuosity is not required to predict accurately the permeability of a packing. For tetrapods with $\Psi = 0.87$ and $\Psi = 0.53$, the permeability was also determined experimentally using the falling head method (green and red crosses in Fig. 10a with the error bars providing the standard deviation based on nine measurements). The experimental results deviate from the LBM results by a factor of 2.3 and 2.8 for $\Psi = 0.87$ and $\Psi = 0.53$,

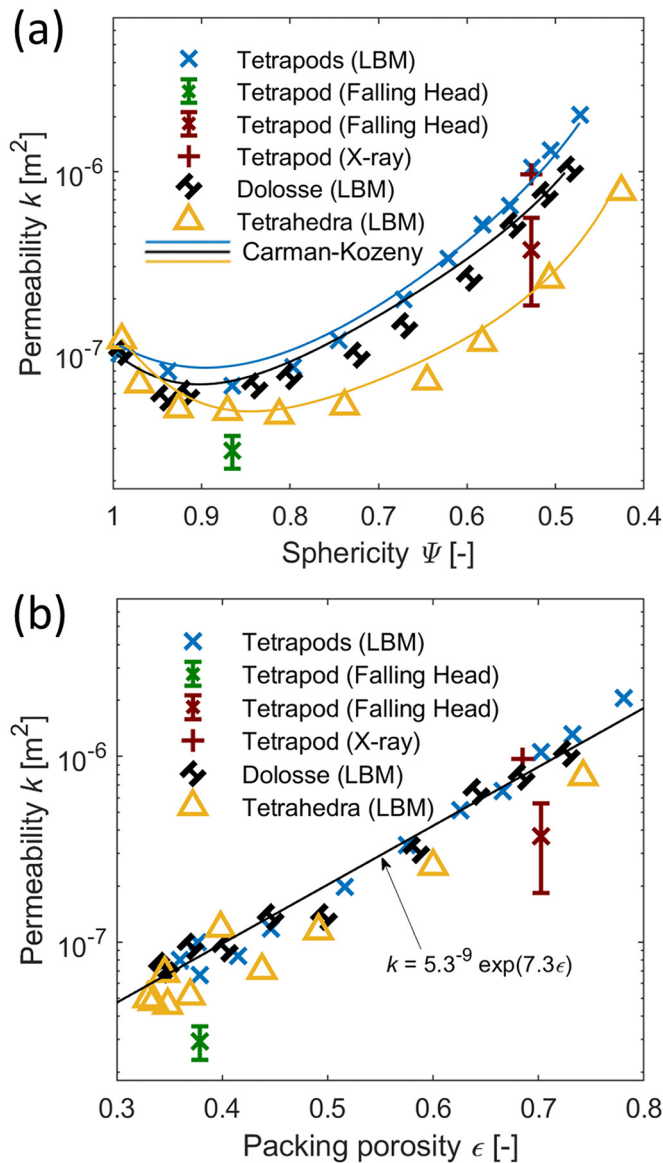


Fig. 10. (a) Permeability of aggregate packings as function of the aggregate sphericity. (b) Permeability as a function of the packing porosity.

respectively. An explanation for this deviation lies presumably in the particularities of the experimental setup, e.g. the wire mesh that is required to keep the packing in position introduces an additional pressure drop. Nevertheless, also the experimental results follow the trend of the k - Ψ behavior of tetrapods as predicted by the Carman-Kozeny correlation and the LBM results. The values of the permeability computed by LBM for a packing of tetrapods with $\Psi = 0.53$ using the packing structure determined either by X-ray CT or DEM differs only by 9%. This excellent agreement indicates that the differences in the permeability obtained from the falling head method and LBM simulations are due to the falling head method instead of differences between the experimental and numerically generated packing structures. Especially for tetrapods with $\Psi = 0.53$ it could be observed during the experiments that the aggregates fall into the mesh with their “arms” sticking out, leading to a local alignment of the aggregates which could increase the packing fraction and therefore increase the pressure drop and in turn decrease the permeability. One way to reduce the differences between the LBM simulations and the permeability experiments could be to including the wire mesh in the numerical simulations to model the additional pressure drop of the mesh itself as well as the influence

of the mesh on the packing structure. Modelling the mesh was omitted in this work as it would be associated with great complexity.

Furthermore, Fig. 10b plots k as a function of ϵ to investigate the correlation between k and ϵ as suggested by the similarity of the k - Ψ and ϵ - Ψ curves. We find that the k - ϵ data can be correlated well ($R^2 = 0.968$) by the function:

$$k = 5.3 \cdot 10^{-9} \exp(7.3\epsilon) \quad (22)$$

Eq. (22) covers a wide range of porosities, shapes and sphericities and is believed to be useful to determine the permeability of packings of aggregates of a known porosity, for aggregates with equivalent diameters similar to the ones studied here. Importantly, Eq. (22) covers both concave and convex particle shapes.

4. Conclusions

This work investigates packings of aggregates spanning a wide range of porosities, i.e. porosities $0.33 < \epsilon < 0.78$. Three types of aggregate structures that is tetrapods, dolosse and tetrahedra are investigated numerically and validated experimentally using two types of tetrapods. The porosity of the packings was determined experimentally and by DEM revealing excellent agreement and providing further evidence for the predictive capabilities of DEM simulations. Importantly, our results show that the packing porosity cannot be predicted directly from the sphericity of the aggregates only, but it also depends on the convexity of the aggregates. The convexity of an aggregate was found to decrease monotonically with decreasing aggregate sphericity for all of the aggregate shapes investigated here. However, the rate of this monotonic decrease depends on the specific aggregate shape.

To investigate whether the aggregate shape affects the morphology of the pore structure, the tortuosity of the packing was determined. We observe that packings of aggregates of different shapes but similar sphericity do not form packings with a similar pore space morphology, as evidenced by a lack of a correlation between the aggregate sphericity and the tortuosity of the packings. Instead, for $\epsilon > 0.35$ a linear correlation was found between the packing porosity and the tortuosity. For $\epsilon < 0.35$ packings of tetrahedra were found to have very high tortuosity, when compared to tetrapods and dolosse. This was attributed to a face-to-face alignment of the closed tetrahedra aggregates. The linear correlation between the tortuosity and the porosity, however, indicates that it is not required to introduce the tortuosity as an additional parameter to determine the permeability of a packing.

Finally, the permeability of the packing was investigated using the LBM and via falling pressure head experiments. The permeability values obtained agree well with the predictions of the Carman-Kozeny correlation, confirming its validity for a wide range of porosities. Since the Carman-Kozeny correlation only depends on the aggregate sphericity Ψ , ϵ and the aggregate diameter, information of a packing's tortuosity is not required to predict its permeability. Furthermore, we propose a correlation that relates the permeability of a packing directly to its porosity. This exponential correlation can be used to determine the permeability of packings of aggregates that are of similar equivalent diameter to the aggregates investigated here. It is hoped that the new insight into the packing of aggregates obtained through this work will pave the way for the development of noise absorbing facades, high permeability pavements for energy harvesting or the mitigation of local heat islands. Regarding the use of artificial aggregates for pavements, future work should consider also the compressive strength as well as the compactibility and workability of aggregate shapes.

Declaration of Competing Interest

The authors declare that they have no known competing financial interests or personal relationships that could have appeared to influence the work reported in this paper.

Acknowledgments

This work has been financed by the Swiss National Science Foundation Grants No. 200021_157122 and 200020_182692.

Appendix A. Supplementary data

Supplementary data to this article can be found online at <https://doi.org/10.1016/j.powtec.2021.11.063>.

References

- [1] B.H. Nam, Z. Behring, J. Kim, M. Chopra, et al., Evaluate the Use of Reclaimed Concrete Aggregate in French Drain Applications, 2014.
- [2] S. Takahashi, M.N. Partl, Improvement of mix design for porous asphalt, *Road Mater. Pavement Des.* 2 (2001) 283–296.
- [3] H. Boler, Y. Qian, E. Tutumluer, Influence of size and shape properties of railroad ballast on aggregate packing, *Transp. Res. Rec. J. Transp. Res. Board.* 2448 (2014) 94–104.
- [4] I. Gruber, I. Zinovic, L. Holzer, A. Flisch, L.D. Poulikakos, A computational study of the effect of structural anisotropy of porous asphalt on hydraulic conductivity, *Constr. Build. Mater.* 36 (2012) 66–77.
- [5] A. Kia, H.S. Wong, C.R. Cheeseman, Clogging in permeable concrete: a review, *J. Environ. Manag.* 193 (2017) 221–233.
- [6] J. Hu, Z. Qian, P. Liu, D. Wang, M. Oeser, Investigation on the permeability of porous asphalt concrete based on microstructure analysis, *Int. J. Pavement Eng.* 1–11 (2019).
- [7] A. García, M.N. Partl, How to transform an asphalt concrete pavement into a solar turbine, *Appl. Energy* 119 (2014) 431–437.
- [8] A.J. Arnfield, Two decades of urban climate research: a review of turbulence, exchanges of energy and water, and the urban heat island, *Int. J. Climatol.* 23 (2003) 1–26.
- [9] A. Chiarelli, A. Al-Mohammedawi, A.R. Dawson, A. García, Construction and configuration of convection-powered asphalt solar collectors for the reduction of urban temperatures, *Int. J. Therm. Sci.* 112 (2017) 242.
- [10] Y. Liu, T. Li, L. Yu, Urban heat island mitigation and hydrology performance of innovative permeable pavement: a pilot-scale study, *J. Clean. Prod.* 244 (2020) 118938.
- [11] T.N. Mansour, B.J. Putman, Influence of aggregate gradation on the performance properties of porous asphalt mixtures, *J. Mater. Civ. Eng.* 25 (2013) 281–288.
- [12] H. Darcy, Les fontaines publiques de la ville de Dijon: Exposition et application... Victor Dalmont, 1856.
- [13] J. Kozeny, Über kapillare Leitung des Wassers im Boden, *R. Acad. Sci. Vienna, Proc. Cl. I* (136) (1927) 271–306.
- [14] P.C. Carman, Fluid flow through granular beds, *Trans. Inst. Chem. Eng.* 15 (1937) 150–166.
- [15] P.C. Carman, *Flow of Gases through Porous Media*, Academic Press, New York, 1956.
- [16] A. Cancelliere, C. Chang, E. Foti, D.H. Rothman, S. Succi, The permeability of a random medium: comparison of simulation with theory, *Phys. Fluids A* 2 (1990) 2085–2088.
- [17] E. Rodriguez, F. Giacomelli, A. Vazquez, Permeability-porosity relationship in RTM for different fiberglass and natural reinforcements, *J. Compos. Mater.* 38 (2004) 259–268.
- [18] N. Henderson, J.C. Brêttas, W.F. Sacco, A three-parameter Kozeny–Carman generalized equation for fractal porous media, *Chem. Eng. Sci.* 65 (2010) 4432–4442.
- [19] R. Zhong, M. Xu, R. Vieira Netto, K. Wille, Influence of pore tortuosity on hydraulic conductivity of pervious concrete: characterization and modeling, *Constr. Build. Mater.* 125 (2016) 1158–1168.
- [20] A. Koponen, M. Kataja, J. Timonen, Permeability and effective porosity of porous media, *Phys. Rev. E - Stat. Physics, Plasmas, Fluids, Relat. Interdiscip. Top.* 56 (1997) 3319–3325.
- [22] G.-C. Cho, J. Dodds, J.C. Santamarina, Particle shape effects on packing density, stiffness, and strength: natural and Crushed Sands, *J. Geotech. Geoenviron. Eng.* 132 (2006) 591–602.
- [23] Y. Jiao, F.H. Stillinger, S. Torquato, Distinctive features arising in maximally random jammed packings of superballs, *Phys. Rev. E* 81 (2010) 041304.
- [24] A.G. Athanassiadis, M.Z. Miskin, P. Kaplan, N. Rodenberg, S.H. Lee, J. Merritt, E. Brown, J. Amend, H. Lipson, H.M. Jaeger, Particle shape effects on the stress response of granular packings, *Soft Matter* 10 (2014) 48–59.
- [25] K. Dierichs, A. Menges, Towards an aggregate architecture: designed granular systems as programmable matter in architecture, *Granul. Matter* 18 (2016) 25.
- [26] K. Murphy, L. Roth, D. Peterman, H. Jaeger, Aleatory construction based on jamming: stability through self-confinement, *Archit. Des.* 87 (2017) 74–81.
- [27] H. Burchard, K. D'Angremond, J. van der Meer, Z. Liu, Empirical formula for breakage of Dolosse and Tetrapods, *Coast. Eng.* 40 (2000) 183–206.
- [28] N.A. Conzelmann, L. Gorjan, F. Sarraf, L.D. Poulikakos, M.N. Partl, C.R. Müller, F.J. Clemens, Manufacturing complex Al₂O₃ ceramic structures using consumer-grade fused deposition modelling printers, *Rapid Prototyp. J.* 26 (2020) 1035–1048.
- [29] K.A. Murphy, N. Reiser, D. Choksy, C.E. Singer, H.M. Jaeger, Freestanding loadbearing structures with Z-shaped particles, *Granul. Matter* 18 (2016) 26.
- [30] S.V. Franklin, Geometric cohesion in granular materials, *Phys. Today* 65 (2012) 70–71.
- [31] N.A. Conzelmann, A. Penn, M.N. Partl, F.J. Clemens, L.D. Poulikakos, C.R. Müller, Link between packing morphology and the distribution of contact forces and stresses in packings of highly nonconvex particles, *Phys. Rev. E* 102 (2020) 062902.
- [32] H.K. Kim, H.K. Lee, Acoustic absorption modeling of porous concrete considering the gradation and shape of aggregates and void ratio, *J. Sound Vib.* 329 (2010) 866–879.
- [33] Y. Zhao, J. Barés, J.E.S. Socolar, Yielding, rigidity, and tensile stress in sheared columns of hexapod granules, *Phys. Rev. E* 101 (2020) 062903.
- [34] P.A. Cundall, O.D.L. Strack, A discrete numerical model for granular assemblies, *Geotechnique* 29 (1979) 47–65.
- [35] G. Lu, J.R.R. Third, C.R.R. Müller, Discrete element models for non-spherical particle systems: from theoretical developments to applications, *Chem. Eng. Sci.* 127 (2015) 425–465.
- [36] G. Lu, J.R. Third, C.R. Müller, Effect of particle shape on domino wave propagation: a perspective from 3D, anisotropic discrete element simulations, *Granul. Matter* 16 (2014) 107–114.
- [37] G. Lu, J.R. Third, C.R. Müller, The parameters governing the coefficient of dispersion of cubes in rotating cylinders, *Granul. Matter* 19 (2017) 12.
- [38] G. Lu, C.R. Müller, Particle-shape induced radial segregation in rotating cylinders, *Granul. Matter* 22 (2020) 50.
- [39] J. Vladimir, Lumelsky, on fast computation of distance between line segments, *Inf. Process. Lett.* 21 (1985) 55–61.
- [40] M. Dawoud, I. Taha, S.J. Ebeid, Effect of processing parameters and graphite content on the tribological behaviour of 3D printed acrylonitrile butadiene styrene, *Mater. Werkst.* 46 (2015) 1185–1195.
- [41] S. Luding, Collisions & Contacts between two particles, in: H.J. Herrmann (Ed.), *Phys. Dry Granul. Media*, Springer Netherlands 1998, pp. 285–304.
- [42] M. Paulick, M. Morgeneyer, A. Kwade, Review on the influence of elastic particle properties on DEM simulation results, *Powder Technol.* 283 (2015) 66–76.
- [43] Y. Yang, J.F. Wang, Y.M. Cheng, Quantified evaluation of particle shape effects from micro-to-macro scales for non-convex grains, *Particuology* 25 (2016) 23–35.
- [44] Persistence of Vision Pty. Ltd., Persistence of Vision Raytracer (Version 3.6) [Computer software], Retrieved from <http://www.povray.org/> 2004.
- [45] J. Latt, O. Malaspinas, D. Kontaxakis, A. Parmigiani, D. Lagrava, F. Brogi, M. Ben Belgacem, Y. Thorimbert, S. Leclaire, S. Li, F. Marson, J. Lemus, C. Kotsalos, R. Conradin, C. Coreixas, R. Petkantchin, F. Raynaud, J. Beny, B. Chopard, Palabos: parallel lattice Boltzmann solver, *Comput. Math. Appl.* 81 (2021) 334–350.
- [46] Z. Guo, B. Shi, N. Wang, Lattice BGK model for incompressible Navier-stokes equation, *J. Comput. Phys.* 165 (2000) 288–306.
- [47] C. Song, P. Wang, H.A. Makse, A phase diagram for jammed matter, *Nature* 453 (2008) 629–632.
- [48] A. Donev, I. Cisse, D. Sachs, E.A. Variano, F.H. Stillinger, R. Connelly, S. Torquato, P.M. Chaikin, Improving the density of jammed disordered packings using ellipsoids, *Science* 303 (2004) 990–993.
- [49] A. Wouterse, S.R. Williams, A.P. Philipse, Effect of particle shape on the density and microstructure of random packings, *J. Phys. Condens. Matter* 19 (2007) 406215.
- [50] C. Ferreira-Córdova, J.S. Van Duineveldt, Random packing of hard spherocylinders, *J. Chem. Eng. Data* 59 (2014) 3055–3060.
- [51] S. Zhao, N. Zhang, X. Zhou, L. Zhang, Particle shape effects on fabric of granular random packing, *Powder Technol.* 310 (2017) 175–186.
- [52] H. Pourtavakoli, E.J.R. Parteli, T. Pöschel, Granular dampers: does particle shape matter? *New J. Phys.* 18 (2016) 73049.
- [53] B. Saint-Cyr, J.-Y. Delenne, C. Voivret, F. Radjai, P. Sornay, Rheology of granular materials composed of nonconvex particles, *Phys. Rev. E* 84 (2011) 041302.
- [54] L. Shen, Z. Chen, Critical review of the impact of tortuosity on diffusion, *Chem. Eng. Sci.* 62 (2007) 3748–3755.
- [55] M. Matyka, A. Khalili, Z. Koza, Tortuosity-porosity relation in porous media flow, *Phys. Rev. E - Stat. Nonlinear, Soft Matter Phys.* 78 (2008) 026306.
- [56] B. Ghanbarian, A.G. Hunt, R.P. Ewing, M. Sahimi, Tortuosity in porous media: a critical review, *soil Sci. Soc. Am. J. Soil Sci. Soc. Am. J.* 77 (2013) 1461–1477.
- [57] S. Khirevich, A. Hölzel, A. Daneyko, A. Seidel-Morgenstern, U. Tallarek, Structure-transport correlation for the diffusive tortuosity of bulk, monodisperse, random sphere packings, *J. Chromatogr. A* 1218 (2011) 6489–6497.
- [58] D.S. Tsai, W. Strieder, Effective conductivities of random fiber bedst, *Chem. Eng. Commun.* 40 (1986) 207–218.
- [59] A. Duda, Z. Koza, M. Matyka, Hydraulic tortuosity in arbitrary porous media flow, *Phys. Rev. E - Stat. Nonlinear, Soft Matter Phys.* 84 (2011) 036319.
- [60] S. Feraie, F.D.E. Latief, Tortuosity-porosity relationship in two-dimensional fractal model of porous media, *Fractals* 21 (2013) 1350013.
- [61] M.R. Smith, L. Collis, Aggregates: Sand, gravel and crushed rock aggregates for construction purposes. 3rd, Geological Society, London, 2001.